

# Plasmonically Enhanced Vibrational Biospectroscopy Using Low-Cost Infrared Antenna Arrays by Nanostencil Lithography

Serap Aksu, Arif E. Cetin, Ronen Adato, and Hatice Altug\*

Plasmonics<sup>[1–8]</sup> is leading to significant advancements and innovations in photonic technologies including biomedicine,<sup>[9,10]</sup> energy harvesting<sup>[11,12]</sup> and telecommunications.<sup>[13]</sup> For biomedical applications, plasmon-based bio nanosensors<sup>[14–17]</sup> consisting of metallic structures could overcome limitations of conventional biosensors through their unique ability to manipulate light at nanoscale dimensions. Plasmonic biosensors could enable detection of medically important proteins and high throughput screening of their interactions.<sup>[18]</sup> One of the powerful and label free optical techniques for determining structural and conformational properties of proteins and protein interactions is Infrared (IR) Spectroscopy.<sup>[19]</sup> However, sensitivity of conventional IR spectroscopy is limited. Thus, relatively large quantities of analytes are required to have sufficient absorption signal. Recently, resonant plasmonic nanoantennas have been used to enhance the absorption signals of surface bound protein monolayers.<sup>[20–25]</sup> The general concept is to electromagnetically couple the vibrational modes of the proteins to the optical modes of the nanoantennas. Plasmonic antennas boost the interaction between the light and the biomolecules through strongly enhanced near fields and increase the sensitivity to attomolar levels.<sup>[26]</sup> Such near field interactions can be controlled through the geometry and composition of the metallic nanostructures in arrays.<sup>[27,28]</sup> Therefore even slight tailoring of the nanoantenna and its arrangement could significantly alter the performance of surface enhanced IR spectroscopy technique. In order to realize precisely tailored plasmonic antennas, highly controllable nanofabrication techniques offering flexible design capability are needed. Conventional electron and ion beam based lithography tools enable tremendous nanoscale feature flexibility. However their limitations such as high operational cost and low throughput have motivated development of new nanofabrication

techniques. There are a few inexpensive innovative approaches demonstrated recently including nano imprinting,<sup>[29]</sup> PEEL (a combination of phase-shifting photolithography, etching, electron-beam deposition and lift-off of the film),<sup>[30]</sup> hole mask colloidal lithography,<sup>[31]</sup> and nano bridging.<sup>[32]</sup> However they either require multiple pattern transfer steps that limits the resolution or they lack the ability of precise arraying and shape control at nanoscale dimensions.

Towards this end, we recently presented that nanostencil lithography (NSL) could be utilized for high resolution, high throughput, and low cost nanofabrication of plasmonic nanoantennas with great design flexibility on conventional as well as flexible and polymeric substrates.<sup>[33,34]</sup> Uniquely, NSL preserves the flexibility of beam based lithography tools for creating nanoantennas in a variety of shapes and arrangements as high-resolution nanostencils are fabricated by e-beam lithography (EBL). We have shown that stencils can be reused multiple times to fabricate series of tailored plasmonic nanoantenna arrays with identical optical responses in a high-throughput fashion.<sup>[34]</sup>

In this work, we present the first demonstration of NSL fabricated low cost nanoantennas for detecting immunologically important, small-sized protein monolayers and perform antibody assays using plasmonically enhanced vibrational biospectroscopy. We show that 3 nm sized protein monolayers could be detected using infrared nanoantennas fabricated by nanostencils. Fabricated arrays consist of precisely arrayed rod shaped gold nanoparticles on a silicon substrate and exploit radiative engineering to achieve strong near field enhancements. Reusable nanostencils enable high throughput and low cost fabrication. However the finite gap between the stencil and the substrate results in small sized gold nanoparticle clusters (5 to 20 nm) around the nanorod antenna due to the diffusion of deposited gold.<sup>[33–36]</sup> Earlier works have shown that these scattered small nanoparticles have no observable perturbation on the far field optical responses.<sup>[34]</sup> Here, we investigate the near field characteristics and biosensing performances of the nanoantennas with such scattered nanoparticles around. We introduced a post-processing method to remove these nanoparticle clusters yielding well-defined nanorod antennas. Our theoretical calculations indicate that small nanoparticles around the nanoantenna enable stronger enhanced near field intensities over larger area compared to the antennas prepared through post-processing. In agreement to these theoretical results, we observe that nanorod antenna arrays directly fabricated using NSL show higher absorption signals for proteins compared to the post-processed ones. This work demonstrates that nanostencil lithography is a promising method for reducing the nano-manufacturing cost while enhancing the performance of biospectroscopy tools for biology and medicine.

Dr. S. Aksu, Prof. H. Altug  
Materials Science and Engineering  
Photonics Center, Boston University  
Boston, MA, 02215, USA  
E-mail: hatice.altug@epfl.ch  
Dr. S. Aksu, Dr. R. Adato, Prof. H. Altug  
Institute of Bioengineering  
School of Engineering  
École Polytechnique Fédérale de Lausanne (EPFL)  
1015 Lausanne, Switzerland  
A. E. Cetin, Dr. R. Adato, Prof. H. Altug  
Electrical and Computer Engineering  
Photonics Center  
Boston University  
Boston, MA, 02215, USA



DOI: 10.1002/adom.201300133

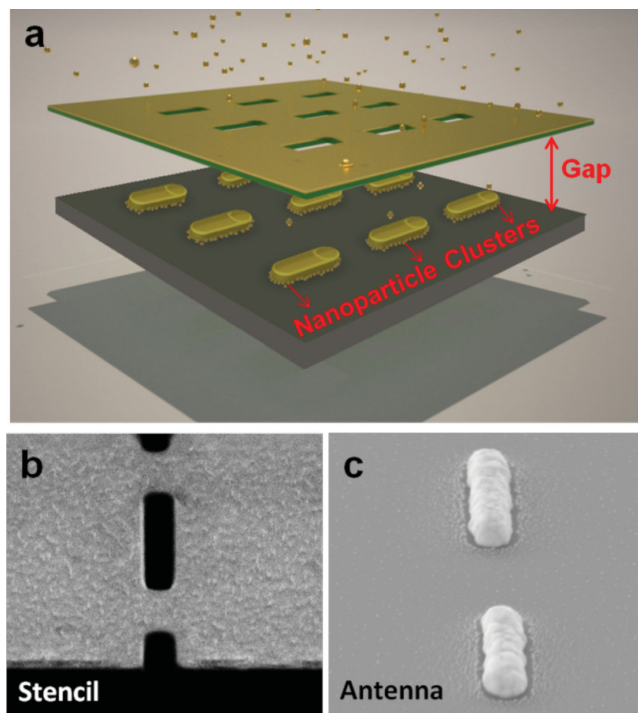


**Figure 1.** Nanostencil lithography is used for low cost nanofabrication of plasmonic antenna arrays. a) Gold deposition scheme is illustrated. Stencil shadows the deposited material. Due to the finite gap between stencil and substrate nanoparticle clusters surround the nanoantennas. b) SEM images of the nanoapertures on the reusable 100 nm thick SiN<sub>x</sub> stencil. Apertures have 1100 nm length and 250 nm width. c) SEM images of gold nanoantennas fabricated on silicon substrate using the nanoapertures shown in (b). Gold nanoparticle clusters are scattered around the nanorods.

Nanostencil lithography is based on shadow mask patterning (Figure 1). Nanostencils placed on any substrate can be used as mask for deposition and implantation of materials<sup>[34]</sup> as well as etching.<sup>[36]</sup> NSL is not a photoresist-based lithography, therefore no solvents, baking or energy radiation is needed. Our nanostencil is composed of nanoapertures that are patterned on 100 nm thick SiN<sub>x</sub> suspended membrane. The stencils are supported by 550 μm thick silicon carrier wafer for easy handling and transfer (see Experimental Section for stencil fabrication). The nanoapertures are defined on the SiN<sub>x</sub> membrane by high resolution EBL and dry etching processes. Nanoapertures used

in this work are patterned over 300 × 300 μm<sup>2</sup> membrane area, which could be easily scaled up to full wafer.<sup>[36]</sup> NSL involves only one single deposition step to create nanostructures on any substrate. The patterned side of the stencil is directly placed on the substrate and secured tightly with mechanical clips to minimize the gap in between.

We deposit gold by electron beam evaporation to fabricate plasmonic nanostructures. Directional deposition of 100 nm thick gold is performed in CHA-600S e-beam evaporator without depositing any prior adhesion layer. Unlike EBL, an adhesion layer is not necessary since NSL does not require a lift-off process. Gold pellets with purity of 99.99% (Kurt J. Lesker Company, USA) are loaded into a 2 cm wide tungsten crucible. The distance between the crucible and stencil is 60 cm. We observed that the pressure inside the evaporator chamber and the gold deposition rate directly influence the resulting antenna quality. Using low pressure (~10<sup>-7</sup>–10<sup>-6</sup> Torr) and low deposition rates (~1 Å/s) reduce the grain size of the deposited gold and enable well defined nanoantennas with smooth surface. After gold deposition, gold remnants on nanostencils can be cleaned using commercially available Gold Etchant TFA (contains 8 wt% iodine, 21 wt% potassium iodide, and 71 wt% water). This cleaning procedure prevents clogging of the stencil and does not damage the nanoapertures. We tested the reusability of the stencils by using three different stencils for 10 times. After cleaning, stencil returns to its initial condition allowing cost efficient nanofabrication.<sup>[37]</sup>

To obtain high resolution plasmonic nanoantennas with nanostencil lithography, the gap between the stencil and the substrate should be minimized. However, there is always an inherent gap in between due to the curvature of the wafers and bending of the stencil membranes. This gap results in scattered gold nanoparticles around the designated structures during the metal deposition step.<sup>[33–36]</sup> Here, we developed a post-processing method to remove these scattered gold nanoparticle clusters. Process involves a dry etching with Argon gas for 20 seconds (10 sccm flow, 35 mTorr pressure and 450 W power) on the patterned silicon substrate. The SEM images of the nanorod arrays before and after processing in Figure 2a and b, respectively, show the effectiveness of dry etch post-processing. As an alternative we also investigated a wet etching based post-processing on the NSL fabricated nanorods using diluted Gold Etchant TFA. The gold etchant is diluted with DI water from 1:1 ratio to 1:15 ratio (TFA:DI) and best results are obtained with 1:12 ratio. We observed that the removal of scattered gold

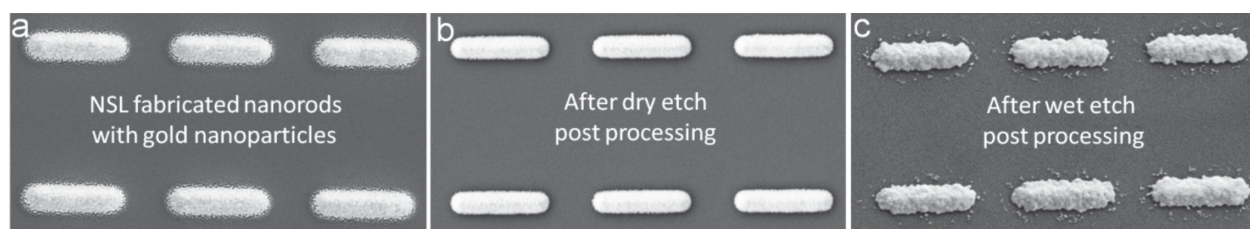


**Figure 2.** SEM images of a) NSL fabricated nanorod antenna arrays. b) and c) show SEM images of nanorod arrays after post-processing with dry etch and wet etch, respectively. Dry etch post-processing is reliable for obtaining well-defined nanostructures with uniform surface. Wet etch post-processing heavily damages the nanorod antenna.

nanoparticles around the antenna is difficult to control with wet etching post-processing and nanorods are heavily damaged as shown in Figure 2c. Therefore, we investigated dry etching as a post-processing method for obtaining well defined nanostructures.

To investigate the use of nanostencil fabricated antennas for increasing infrared absorption signal of proteins, the suitable nanorod dimensions are first determined theoretically by tailoring the length and the periodicity. Maximum enhanced near fields as well as the best spectral overlap of plasmonic excitations with vibrational bands of the protein backbone around  $6\ \mu\text{m}$  wavelength is achieved using  $1100\ \text{nm}$  long and  $250\ \text{nm}$  wide nanorods with  $1.6\ \mu\text{m}$  periodicity in a  $50 \times 50$  particle array of square lattice. The far- and near-field responses of nanorod antennas are analyzed by finite-difference time-domain (FDTD) solver Lumerical Solutions. The dielectric constants of gold and silicon are taken from Palik's Handbook of Optical Constants. Periodic boundary conditions were used along  $x$ - and  $y$ - directions. Light is normally incident on the structures along the  $z$  axis. Along the direction of the illumination source ( $z$ ), perfectly matched layer boundary condition was applied. In the simulations, the mesh size is set  $2\ \text{nm}$  along the  $x$ ,  $y$ , and  $z$  directions. We performed simulations on NSL fabricated and post-processed nanorod antenna arrays with determined geometrical parameters and compared their near field intensity enhancements at  $6\ \mu\text{m}$  wavelength. NSL fabricated nanorods are designed by imitating the SEM images where nanorod is generated as a half cylinder attached to half hemispheres on both ends. Nanoparticles with  $10$  to  $20\ \text{nm}$

size are randomly placed around the nanorod at the substrate air interface (Figure 3a). To investigate the effect of spatial distribution of gold nanoparticles around the antenna, simulations with different nanoparticle arrangements have been performed. It is observed that each design has similar near field enhancements. For simulations of post-processed nanorods, the tiny gold nanoparticle clusters around the nanorod are removed (Figure 3b). In Figure 3, left column shows the near field intensity distribution at silicon-gold interface of a) NSL fabricated and b) post-processed nanorods. Field enhancement of NSL fabricated nanorods is an order of magnitude higher compared to post-processed ones. These calculations indicate that nanoparticles around the antenna behave as light scattering sites and contribute to the near field enhancement of the antenna.

In Figure 3 the near field intensity distributions are plotted with the same color scale for two different nanorods. We observed that for the antenna with scattered gold nanoparticles around, not only the maximum intensity is higher but also the field-enhanced area on silicon-gold interface is larger. We calculated the field-enhanced area at gold-silicon interface ( $z = 0$ ) for two different nanorods using the simulation design shown in Figure 3. For calculations we defined a cut-off field intensity value as  $1/e^2$  of the maximum intensity on post-processed nanorods since this nanorod yields lower field intensity. We then sum up the area where the field intensity is higher than this cut-off value. The calculated field enhanced area is two times higher for NSL fabricated nanorods ( $1.9 \times 10^4\ \text{nm}^2$ ) than that of the post-processed ( $1 \times 10^4\ \text{nm}^2$ ) ones.

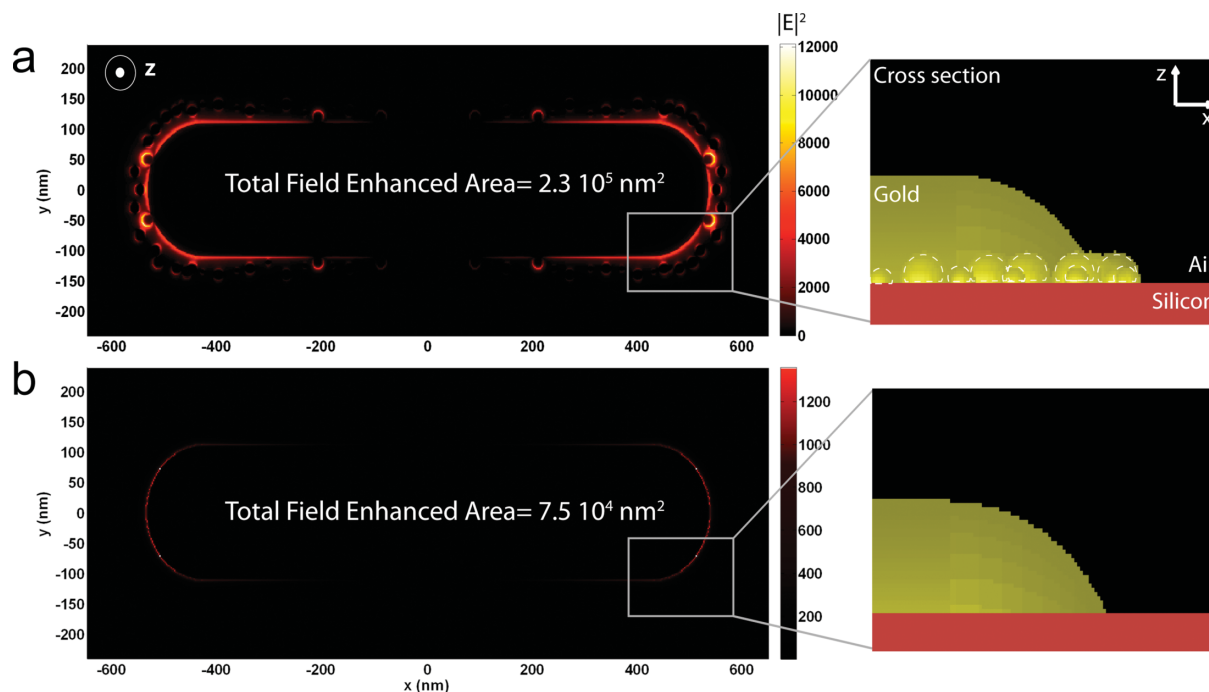


**Figure 3.** Finite-difference time-domain calculations on a) NSL fabricated b) post-processed nanorod antenna arrays. NSL fabricated nanorods are simulated by incorporating nanorods with tiny nanoparticles ( $10$  and  $20\ \text{nm}$  diameter) at the gold-silicon interface ( $z = 0$ ). On the left column, field intensity distributions are shown at  $z = 0$ , at  $6\ \mu\text{m}$  wavelength for both antenna arrays. NSL fabricated nanorods show an order of magnitude higher field enhancement. The total field-enhanced area calculated around the three-dimensional structures is three times larger for NSL fabricated nanorods. The right column shows the cross sections ( $y = 0$ ) of the simulated designs.

Given that the nanorods and the tiny nanoparticles are 3D objects, proteins can bind at their curved surfaces. Therefore we extended the calculation of enhanced area (as described above) along the  $z$  direction as follows. In the calculations, step size on the  $z$ -axis is set as mesh size (2 nm). The field-enhanced area at each  $z$  value (0, 2, 4 nm...) is calculated and these areas are summed up to obtain the total region with field enhancements higher than the selected cutoff intensity. The calculated total area for NSL fabricated nanorods is three times larger than the post-processed nanorods ( $2.3 \times 10^5 \text{ nm}^2$  versus  $7.5 \times 10^4 \text{ nm}^2$ ). Given that the detection sensitivity in spectroscopy is linearly proportional with the amount of molecules and the enhanced fields overlapping with them, theoretical calculations indicate that NSL fabricated antennas with scattered nanoparticles are highly advantageous.

In order to demonstrate NSL fabricated low cost nanorod antennas for plasmonically enhanced infrared biospectroscopy, we tested the system with protein monolayer and antibody immobilized bilayers as near field probes. First Protein A/G (Thermo Scientific Pierce) monolayer is physisorbed to the gold nanoantenna substrates (see Experimental Section) forming a monolayer. Protein A/G, which is a recombinant fusion protein constituting binding domains of both protein A and protein G with molecular weight of 50.46 kDa, has a strong affinity with Fc regions of antibodies. Thickness of a monolayer on gold is measured as  $\sim 3$  nm by ellipsometry.<sup>[38]</sup> Then anti-mouse IgG from goat (T6653 Sigma Aldrich) are immobilized on protein A/G monolayer. Molecular weight of IgG is 140 kDa. An additional 5 nm thick layer of IgG is detected by ellipsometry. Detecting the protein signatures of monolayer and antibody bilayer is achieved by measuring the reflection spectrum of nanorod antenna arrays before and after protein binding. The optical set-up consists of an IR microscope coupled to a Bruker Fourier Transform Infrared (FTIR) spectrometer with a KBr beam splitter. Polarized light (along the nanorod) is normally incident on the nanorod-patterned surface. Reflected infrared signal from antenna arrays is collected using a Cassegrain reflection optics (N.A. = 0.4) and coupled into a mercury cadmium telluride (MCT) detector. The collected signal is normalized with the reflection signal from a reference mirror.

The overlap of the plasmonic resonance with absorption bands of protein results in dips in the reflectance spectra where the strength of the dip is directly correlated with enhancement of the protein absorption signal.<sup>[39]</sup> In **Figure 4a** and **b** the reflection spectra before binding any proteins (black dotted curve), after Protein A/G binding (blue curve) and after antibody immobilization (red curve) on the NSL fabricated and post-processed nanorods, respectively, are shown. In these figures, the dips indicated by vertical dashed lines at amide I (orange, at  $1660 \text{ cm}^{-1}$ ) and amide II (green, at  $1540 \text{ cm}^{-1}$ ) vibrational frequencies are clearly noticeable within the optical spectra collected from the protein coated antenna arrays. Even though protein A/G is a relatively small molecule, NSL fabricated antennas could clearly resolve amide absorption bands. After antibody immobilization, a stronger dip on the plasmonic resonances is observed due to the larger biomass of antibody. To determine the amount of protein absorption signal, the dips in the reflectance spectra are quantified by subtracting the spectra of protein A/G monolayer and antibody bilayers from

the initial spectra of nanorod antennas before protein binding ( $\Delta R = R_{\text{before}} - R_{\text{after}}$ ). Loading the antenna with protein layers results in a slight red shift on plasmonic resonance and this shift is corrected for calculating the difference spectrum ( $\Delta R$ ).

**Figure 4c** and **d** show the difference spectrum of protein A/G monolayer and antibody (IgG) bilayers on the NSL fabricated and post-processed arrays, respectively. The absorption signals of proteins appearing as two peaks (amide I at  $1660 \text{ cm}^{-1}$  and amide II at  $1540 \text{ cm}^{-1}$ ) are above the noise level for both arrays. As shown in **Figure 4c**, the magnitude of the amide I absorption signal of protein A/G on NSL fabricated antennas (0.012) is nearly three times higher than that of the post-processed antennas (0.004). Similarly, **Figure 4d** shows the protein absorption signal after antibody immobilization. Absorption signal for protein A/G- antibody bilayer is doubled compared to protein A/G monolayer for both NSL fabricated and post-processed nanorods due to the introduction of larger antibody. The magnitude of the amide I absorption signal of antibody on NSL fabricated antennas (0.025) is nearly three times higher than that of the post-processed antennas (0.009). Removing the nanoparticles around the nanorods using a post-processing reduces the absorption signal for both protein A/G and antibody. These experimental results are in very good agreement with our numerical calculations, which indicate nearly three times larger enhanced surface area for NSL fabricated nanorods. To quantify the enhancement factor provided by the nanoantennas, we performed IR reflection absorption spectroscopy (IRRAS).<sup>[21,26,40–42]</sup> IRRAS measurements are performed at a grazing angle ( $80^\circ$ ) for protein A/G monolayer and antibody bilayer coated 100 nm thick gold films. Enhancement factor calculations are performed by comparing the expected difference signal obtained from a 3 nm thick protein A/G monolayer (0.013%) using IRRAS measurements to the experimentally measured one (1.2%). In addition, we take into account that the observed enhanced signal is only due to the molecules present on the field-enhanced area.<sup>[26]</sup> For NSL fabricated nanorods with nanoparticle clusters around, we calculated field-enhanced area as  $\sim 2.3 \times 10^5 \text{ nm}^2$  for one unit cell as indicated before. The fabricated arrays that are used for experimental measurements contain  $50 \times 50$  rods. For the experimental testing the spot size of the incident beam is set as the size of the array ( $80 \times 80 \mu\text{m}^2$ ). Therefore fraction of the active area for an array to the total incident beam is  $\sim 8.9 \times 10^{-3}$ . Accordingly, scaling the ratio of our measured signal to the estimated difference absorption signal with the area factor yields an enhancement factor of 10300. These measurements and calculations demonstrate NSL fabricated low cost nanorod antenna arrays with gold nanoparticle clusters can enhance the protein signals significantly and serve as sensitive biospectroscopy substrates.

In this work we present the first demonstration of Nanos-tencil Lithography fabricated low cost infrared nanoantenna arrays for plasmonically enhanced vibrational biospectroscopy application. Specifically we show detection of 3 nm sized protein monolayers and perform antibody assays using precisely arrayed nanoantennas fabricated by reusable stencils. Due to the inherent gap between the stencil and rigid surface resulting from curved surfaces, we observed tiny metallic nanoparticle clusters around the antenna. We presented a post-processing method to effectively remove these gold nanoparticle clusters without damaging the antenna surface. Our experimental results show that antennas directly fabricated with NSL gives

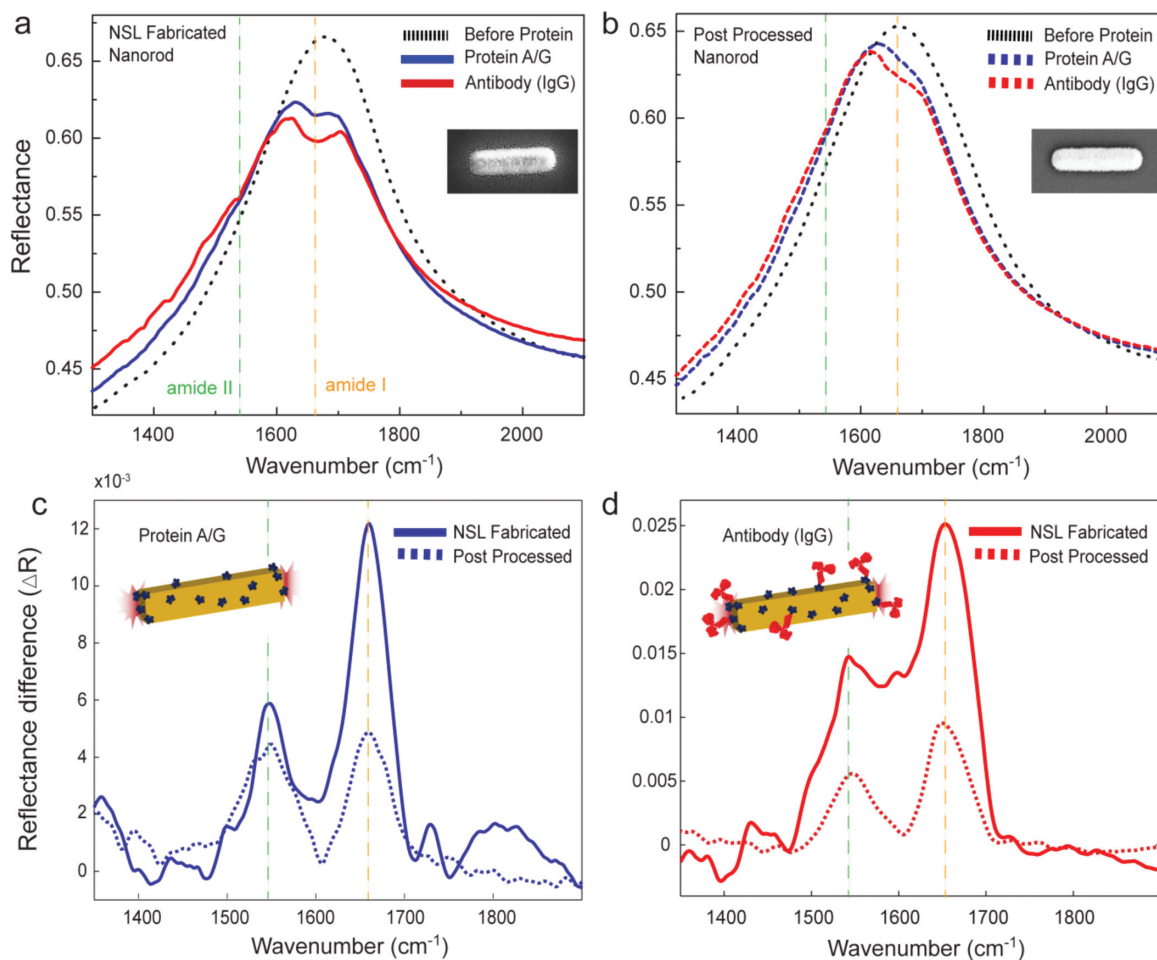


**Figure 4.** Plasmonically enhanced biospectroscopy of protein A/G monolayer and antibody (IgG) is shown. a) Reflectance spectra of NSL fabricated nanorods before protein binding (black dotted curve), after protein A/G (blue solid) and after antibody (red solid) are shown. Light is polarized along the nanorods for all measurements. Dips as a result of amide I (at  $1660\text{ cm}^{-1}$ ) and amide II (at  $1540\text{ cm}^{-1}$ ) absorption bands are indicated with orange and green vertical dashed lines, respectively. Inset shows SEM image of NSL fabricated nanorod. b) Reflectance spectra of post-processed nanorod antenna arrays before and after protein binding are shown. After antibody immobilization stronger dip is observed for both NSL fabricated and post-processed nanorods. Inset shows the SEM image of the post-processed nanorod. c) Reflectance difference between the spectra of nanorod antennas before and after protein A/G binding is shown for both nanorods. Peaks appear at amide I and amide II bands of protein A/G. Peaks here correspond to the dips in a) and b). Signal due to amide I is almost three times higher for NSL fabricated nanorods. d) Reflectance difference after antibody binding (IgG) on protein A/G is shown for both nanorods. Similarly, signal due to amide I is almost three times higher for NSL fabricated nanorods. Insets of (c) and (d) illustrate protein A/G monolayer and protein A/G-antibody bilayer on nanorods.

nearly three times higher protein absorption signal than that of post-processed nanoantennas. This observation is supported by theoretical calculations indicating the nanoparticle clusters enable near-field enhancements over almost three times larger area. The presented results demonstrate that nanostencil lithography is a promising technique for reducing the nanomanufacturing cost while enhancing the performance of biospectroscopy tools for biology and medicine. As a single-step and low cost nanofabrication technique, NSL could facilitate the manufacturing of biophotonic technologies for real-world applications.

## Experimental Section

*Nanostencil and Structure Fabrication:*<sup>[34]</sup> Nanostencil technique consists of three stages: (i) fabrication of the free-standing membrane,

(ii) patterning on the membrane and (iii) direct deposition of metallic plasmonic devices. We start with  $550\text{ }\mu\text{m}$  thick silicon wafer coated with  $400\text{ nm}$  thick LPCVD  $\text{SiN}_x$  on double sides. After cleaning with organic solvents,  $2\text{ }\mu\text{m}$  thick MICROPOSIT S1818 positive photoresist is spin coated.  $800\text{ }\mu\text{m} \times 800\text{ }\mu\text{m}$  apertures on the  $\text{SiN}_x$  layer are defined by photolithography with SUSS MicroTec MA/BA6 Mask Aligner and reactive ion etching (RIE) with Plasma Therm 790 RIE/PECVD System. Then, the chips are immersed in KOH solution to selectively etch Si layer. Finally,  $\sim 200\text{ }\mu\text{m} \times 200\text{ }\mu\text{m}$  and  $400\text{ nm}$  thick free-standing  $\text{SiN}_x$  membranes are obtained once the etching stops at the  $\text{SiN}_x$  layer. Si is etched with  $54.7^\circ$  angle sidewall profile. The second stage is nanoaperture patterning on the membrane. This process involves spinning positive e-beam resist poly (methylmethacrylate) (PMMA) followed by e-beam exposure using Zeiss Supra 40VP with GEMINI electron-optics column. Here, the EBL process is needed only once for the creation of the mask, since the mask can be used multiple times. After development of PMMA resist, patterns are transferred to the  $\text{SiN}_x$  membrane by RIE using  $\text{SF}_6$  and Ar gases. The resulting structure is used as stencil. The final stage of nanostencil

method involves direct deposition of the plasmonic structures to the desired surface. The stencil is directly placed on the substrate and secured tightly with clips while the patterned SiN<sub>x</sub> layer is nominally kept in contact with the substrate. Here, the sturdiness of the LPCVD SiN<sub>x</sub> layer plays important role for the durability of the mask. Directional gold deposition at  $3 \times 10^{-6}$  Torr is performed in CHA-600S e-beam evaporator for 100 nm gold film without depositing any prior adhesion layer. When the mask is removed from the substrate, it leaves plasmonic nanostructures on the substrate with the shapes complementary to the nanoapertures.

**Optical Characterization:** The reflectance data on the nanorod antenna arrays was collected using an FTIR spectrometer (Bruker, IFS 66/s) and infrared microscope (Bruker, Hyperion 1000). The sample spectra are normalized to the reflectance spectra obtained from a reference mirror. All spectra are collected at a resolution of  $4 \text{ cm}^{-1}$  and consist of 256 scans co-added with a scanner velocity of 40 kHz. Spectroscopic scans are performed under a dry air purged environment to eliminate atmospheric absorption. The thickness of the protein layers was independently characterized through ellipsometer (variable-angle spectroscopic ellipsometer, Woollam) measurements. We obtained thicknesses of 2.85 and 7.92 nm for the protein A/G, protein A/G-IgG bilayer respectively. The IgG thickness is obtained as  $\sim 5.10$  nm.

**Monolayer Chemistry and Preparation:** Before surface functionalization, nanorod antenna patterned silicon chips were cleaned in Plasma Asher with oxygen environment for 10 min. Protein A/G at a concentration of  $1 \text{ mg mL}^{-1}$  in PBS (10 mM phosphate buffer) was spotted on the substrate surface and incubated for 1 h. A post-incubation wash was carried out to remove unbound protein. To form a protein bilayer of A/G and IgG, IgG (anti-mouse from goat) proteins at a concentration of  $1 \text{ mg mL}^{-1}$  in PBS was subsequently spotted on the protein A/G-coated nanorod antennas and left to incubate again for 1 h. A second post-incubation wash was then carried out.

## Acknowledgments

We thank Pinar Dursun for illustrations. This research was supported by the Office of Naval Research (11PR00755–00-P00001) and NSF CAREER Award (ECCS-0954790) to H.A.

Received: March 4, 2013

Revised: June 28, 2013

Published online: July 25, 2013

- [1] B. Luk'yanchuk, N. Zheludev, S. A. Maier, N. J. Halas, P. Nordlander, H. Giessen, C. T. Chong, *Nat. Mater.* **2010**, *9*, 707.
- [2] S. Law, V. Podolskiy, D. Wasserman, *Nanophotonics* **2013**, DOI 10.1515/nanoph-2012-0027
- [3] H. Cansizoglu, M. F. Cansizoglu, M. Finckenor, T. Karabacak, *Adv. Optical Mater.* **2013**, *1*, 2.
- [4] C. Estevez, J. Belenguer, S. Gomez-Montes, J. Miralles, A. M. Escuela, A. Montoya, L. M. Lechuga, *Analyst* **2012**, *137*, 5659.
- [5] K. Aydin, V. E. Ferry, R. M. Briggs, H. A. Atwater, *Nature Commun.* **2011**, *2*, 517.
- [6] A. Kinkhabwala, Z. Yu, S. Fan, W. E. Moerner, *Chem. Phys.* **2012**, *1*, 406.
- [7] B. Khademhosseini, G. Biener, I. Sencan, T. Su, A. F. Coskun, A. Ozcan, *Appl. Phys. Lett.* **2010**, *97*, 221107.
- [8] R. Zia, *Nature Photon.* **2008**, *2*, 213.
- [9] R. Bardhan, S. Lal, A. Joshi, N. J. Halas, *Acc. Chem. Res.* **2011**, *44*, 936.
- [10] E. Y. Lukianova-Hleb, X. Ren, J. A. Zasadzinski, X. Wu, D. O. Lapotko, *Adv. Mater.* **2012**, *24*, 3831.
- [11] A. Aubry, D. Y. Lei, A. I. Fernández-Domínguez, Y. Sonnefraud, S. A. Maier, J. B. Pendry, *Nano Lett.* **2010**, *10*, 2574.
- [12] A. Polman, H. A. Atwater, *Nat. Mater.* **2012**, *11*, 174.
- [13] M. A. Noginov, L. Gu, J. Livenere, G. Zhu, A. K. Pradhan, R. Mundle, M. Bahoura, Y. A. Barnakov, V. A. Podolskiy, *Appl. Phys. Lett.* **2011**, *99*, 021101.
- [14] S. S. Accímovicć, M. P. Kreuzer, M. U. González, R. Quidant, *ACS Nano* **2009**, *3*, 1231.
- [15] J. C. Reed, H. Zhu, A. Y. Zhu, C. Li, E. Cubukcu, *Nano Lett.* **2012**, *12*, 4090.
- [16] J. N. Anker, W.P. Hall, O. Lyandres, N. C. Shah, J. Zhao, R. P. Van Duyne, *Nat. Mater.* **2008**, *7*, 442.
- [17] A. B. Dahlin, S. Chen, M. P. Jonsson, L. Gunnarsson, M. Kall, F. Hook, *Anal. Chem.* **2009**, *81*, 6572.
- [18] T.-Y. Chang, M. Huang, A. A. Yanik, H.-Y. Tsai, P. Shi, S. Aksu, M. F. Yanik, H. Altug, *Lab Chip* **2011**, *11*, 3596.
- [19] K. J. Ewing, L. B. Shaw, R. Kim, R. R. Gattass, J. Sanghera, I. Aggarwal, *Proc. SPIE* **2011**, *8018*, 80180U.
- [20] F. Le, D. W. Brandl, Y. A. Urzhumov, H. Wang, J. Kundu, N. J. Halas, J. Aizpurua, P. Nordlander, *ACS Nano* **2008**, *2*, 707.
- [21] F. Neubrech, A. Pucci, T. W. Cornelius, S. Karim, A. Garcia Etxarri, J. Aizpurua, *Phys. Rev. Lett.* **2008**, *101*, 157403.
- [22] I. M. Pryce, Y. A. Kelaita, K. Aydin, H. A. Atwater, *ACS Nano* **2011**, *5*, 8167.
- [23] N. H. Kim, S. J. Lee, M. Moskovits, *Nano Lett.* **2010**, *10*, 4181.
- [24] E. J. Smythe, M. D. Dickey, J. Bao, G. M. Whitesides, F. Capasso, *Nano Lett.* **2009**, *9*, 1132.
- [25] V. Liberman, R. Adato, A. Mertiri, A. A. Yanik, K. Chen, T. H. Jeys, S. Erramilli, H. Altug, *Opt. Express* **2011**, *19*, 11202.
- [26] R. Adato, A. A. Yanik, J. J. Amsden, D. L. Kaplan, F. G. Omenetto, M. K. Hong, S. Erramilli, H. Altug, *Proc. Natl. Acad. Sci. USA* **2009**, *106*, 19227.
- [27] L. Novotny, N. Hulst, *Nature Photon.* **2011**, *5*, 83–90.
- [28] N. Liu, M. L. Tang, M. Hentschel, H. Giessen, A. P. Alivisatos, *Nat. Mater.* **2011**, *10*, 631.
- [29] S. Zankovych, T. Hoffmann, J. Seekamp, J.-U. Bruch, C. M. Sotomayor Torres, *Nanotechnology* **2001**, *12*, 91.
- [30] J. Henzie, M. Hyung Lee, T. W. Odom, *Nature Nanotechnol.* **2007**, *2*, 549.
- [31] S. Cataldo, J. Zhao, B. Frank, F. Neubrech, C. Zhang, P. V. Braun, H. Giessen, *ACS Nano* **2012**, *6*, 979.
- [32] D.-K. Lim, K.-S. Jeon, J.-H. Hwang, H. Kim, S. Kwon, Y. D. Suh, J. M. Nam, *Nat. Nanotechnol.* **2011**, *6*, 452.
- [33] S. Aksu, M. Huang, A. Artar, A. A. Yanik, S. Selvarasah, M. Dokmeci, H. Altug, *Adv. Mater.* **2011**, *23*, 4422.
- [34] S. Aksu, A. A. Yanik, R. Adato, A. Artar, M. Huang, H. Altug, *Nano Lett.* **2010**, *10*, 2511.
- [35] O. Vazquez-Mena, T. Sannomiya, M. Tosun, L.G. Villanueva, V. Savu, J. Voros, J. Brugger, *ACS Nano* **2012**, *6*, 5474.
- [36] O. Vazquez-Mena, L. G. Villanueva, V. Savu, K. Sidler, M. A. F. van den Boogaart, J. Brugger, *Nano Lett.* **2008**, *8*, 3675.
- [37] M. Huang, B. C. Galarreta, A. Artar, R. Adato, S. Aksu, H. Altug, *Nano Lett.* **2012**, *12*, 4817.
- [38] C. W. Wu, A. B. Khanikaev, R. Adato, N. Arju, A. A. Yanik, H. Altug, G. Shvets, *Nat. Mater.* **2012**, *11*, 69.
- [39] V. Giannini, Y. Francescato, H. Amrania, C. C. Phillips, S. A. Maier, *Nano Lett.* **2011**, *11*, 2835.
- [40] D. Enders, A. Pucci, *Appl. Phys. Lett.* **2006**, *88*, 184104.
- [41] F. Neubrech, A. Pucci, *IEEE J. Selected Topics Quantum Electron.* **2013**, *19*, 3.
- [42] J. Kundu, F. Le, P. Nordlander, N. J. Halas, *Chem. Phys. Lett.* **2008**, *452*, 119.